

Criteria for the formation of Population III objects in the ultraviolet background radiation

T. Kitayama,¹★ H. Susa,² M. Umemura² and S. Ikeuchi³

¹*Department of Physics, Tokyo Metropolitan University, Hachioji, Tokyo 192-0397, Japan*

²*Center for Computational Physics, University of Tsukuba, Tsukuba 305-8577, Japan*

³*Department of Physics, Nagoya University, Chikusa-ku, Nagoya 464-8602, Japan*

Accepted 2001 May 15. Received 2001 April 5; in original form 2000 December 11

ABSTRACT

We explore possibilities of collapse and star formation in Population III objects exposed to the external ultraviolet background (UVB) radiation. Assuming spherical symmetry, we solve self-consistently radiative transfer of photons, non-equilibrium H₂ chemistry and gas hydrodynamics. Although the UVB does suppress the formation of low-mass objects, the negative feedback turns out to be weaker than previously suggested. In particular, the cut-off scale of collapse drops significantly below the virial temperature $T_{\text{vir}} \sim 10^4$ K at weak UV intensities ($J_{21} \lesssim 10^{-2}$), owing to both self-shielding of the gas and H₂ cooling. Clouds above this cut-off tend to contract highly dynamically, further promoting self-shielding and H₂ formation. For plausible radiation intensities and spectra, the collapsing gas can cool efficiently to temperatures well below 10^4 K before rotationally supported and the final H₂ fraction reaches $\sim 10^{-3}$.

Our results imply that star formation can take place in low-mass objects collapsing in the UVB. The threshold baryon mass for star formation is $\sim 10^9 M_{\odot}$ for clouds collapsing at redshifts $z \lesssim 3$, but drops significantly at higher redshifts. In a conventional cold dark matter universe, the latter coincides roughly with that of the 1σ density fluctuations. Objects near and above this threshold can thus constitute ‘building blocks’ of luminous structures, and we discuss their links to dwarf spheroidal/elliptical galaxies and faint blue objects. These results suggest that the UVB can play a key role in regulating the star formation history of the Universe.

Key words: molecular processes – radiative transfer – galaxies: formation – cosmology: theory – diffuse radiation.

1 INTRODUCTION

The existence of an intense ultraviolet background (UVB) radiation, inferred from observations of QSO absorption spectra (Gunn & Peterson 1965; Bajtlik, Duncan & Ostriker 1988), is likely to have prominent impacts on galaxy formation. While its origin could be attributed to QSOs or young galaxies appearing at high redshifts (e.g. Couchman 1985; Miralda-Escudé & Ostriker 1990; Sasaki & Takahara 1994; Fukugita & Kawasaki 1994), the UVB, once produced, photoionizes the intergalactic medium and alters the subsequent growth of cosmic structures. These secondary structures that have emerged in the UVB are further responsible for producing the radiation field, which can in turn affect the development of next generation objects. It is therefore crucial to determine quantitatively the consequences of radiative feedback on

the formation of early generation (hereafter Population III) objects, in order to link the build-up of structures with the thermal history of the Universe.

It has long been suggested that the formation of subgalactic objects is suppressed via photoionization and heating caused by the UVB (Umemura & Ikeuchi 1984; Ikeuchi 1986; Rees 1986; Bond, Szalay & Silk 1988; Efstathiou 1992; Babul & Rees 1992; Murakami & Ikeuchi 1993; Chiba & Nath 1994; Zhang, Anninos & Norman 1995; Thoul & Weinberg 1996, among others). Most previous studies, however, assumed for simplicity that the medium is optically thin against the external radiation. Several attempts have been made recently to take into account radiative transfer of photons (e.g. Kepner, Babul & Spergel 1997; Tajiri & Umemura 1998; Abel, Norman & Madau 1999; Barkana & Loeb 1999; Razoumov & Scott 1999; Gnedin 2000b; Susa & Umemura 2000a; Nakamoto, Umemura & Susa 2001; Ciardi et al. 2001). In our previous papers (Kitayama & Ikeuchi 2000, hereafter Paper I;

★E-mail: tkita@phys.metro-u.ac.jp

Kitayama et al. 2000, hereafter Paper II), we have studied the evolution of spherical clouds exposed to the UVB, explicitly solving radiative transfer of ionizing photons and hydrodynamics. We have found that the collapse of objects with circular velocities below $V_c \sim 15\text{--}40\text{ km s}^{-1}$ can be prohibited completely even if self-shielding of gas is taken into account. We have also noted that a spherical cloud above this threshold undergoes runaway collapse in the dark matter potential and does not settle into hydrostatic equilibrium. For plausible intensities and spectra of the UVB, the central region of such a cloud is shown to become self-shielded against photoionization before shrinking to the rotation barrier. A question still remains as to whether star formation can take place efficiently in the cloud collapsing under the UVB.

A key element in this context is molecular hydrogen (H_2). In order for stars to form, the gas needs to radiate energy efficiently and cool down to temperatures well below $T = 10^4\text{ K}$. In the gas of primordial composition without metals, cooling processes at this temperature are almost solely dominated by rotational–vibrational line excitation of H_2 (e.g. Peebles & Dicke 1968; Hirasawa 1969; Matsuda, Sato & Takeda 1969). Formation and destruction of H_2 , however, are very sensitive to the presence of a radiation field. For instance, H_2 molecules are easily dissociated by photons in the so-called Lyman–Werner (LW, 11.2–13.6 eV) bands (Stecher & Williams 1967; Haiman, Rees & Loeb 1997; Ciardi et al 2000b; Machacek, Bryan & Abel 2001) or via collisions with ions. On the other hand, the gas-phase formation of H_2 is promoted by an enhanced ionized fraction in the post-shock gas (Shapiro & Kang 1987; Kang & Shapiro 1992) or in weakly photoionized media (Haiman, Rees & Loeb 1996b). In addition, self-shielding taking place during dynamical collapse can also aid H_2 cooling (Susa & Kitayama 2000). It is thus by no means trivial to determine in what circumstances the UVB has positive or negative feedback on star formation in Population III objects.

In this paper, by including H_2 chemistry consistently with radiative transfer of UV photons, we extend our previous analyses (Papers I and II) and study the fate of Population III objects exposed to the external UVB. Assuming spherical symmetry, we solve the radiative transfer equation, non-equilibrium chemical reactions including H_2 formation and destruction, and dynamics of baryonic gas and dark matter. Particular attention is paid to the possibilities of both collapse and H_2 cooling in the presence of UV radiation fields. We explore the evolution of objects with wide ranges of masses, including those with the virial temperature $T_{\text{vir}} < 10^4\text{ K}$ ($V_c < 17\text{ km s}^{-1}$), which have been left out in our previous analyses neglecting H_2 formation. A similar problem was investigated earlier by Kepner et al. (1997) and Haiman, Abel & Rees (2000), assuming that collapsed clouds are in approximate hydrostatic equilibrium. As mentioned above and shown explicitly in this paper, the gas in collapsed objects is far from static and its physical state changes highly dynamically. We also note that our analysis is complementary to that of Susa & Umemura (2000a,b), who explored the pregalactic pancake collapse in plane-parallel geometry and studied the fate of objects far above the Jeans scale. We pay particular attention to the development of smaller objects near the Jeans scale, which are likely to evolve spherically to a first-order approximation. A crucial distinction between the earlier works and ours is that the gas density rises rapidly along with the spherical collapse, in proportion to the cube of scalelength, providing greater chances of self-shielding and H_2 cooling.

This paper is organized as follows. Section 2 describes the numerical model used in the paper. We present the simulation results in Section 3 and discuss their implications on galaxy

formation in Section 4. Finally, Section 5 summarizes our conclusions. Throughout the paper, we assume the density parameter $\Omega_0 = 0.3$, the cosmological constant $\lambda_0 = 0.7$, the Hubble constant $h_{100} = H_0/(100\text{ km s}^{-1}\text{ Mpc}^{-1}) = 0.7$, and the baryon density parameter $\Omega_b = 0.05$.

2 MODEL

2.1 Numerical scheme

We simulate the evolution of a spherically symmetric cloud exposed to the external UVB. The cloud is a mixture of baryonic gas and dark matter with the mass ratio of $\Omega_b : \Omega_0 - \Omega_b = 1 : 5$. The basic equations are summarized in Section 2.1 of Paper I. One modification is that the acceleration term arising from the cosmological constant $+\lambda_0 H_0^2 r$ is added to the right-hand side of the momentum equations. They are solved with the second-order-accurate Lagrangian finite-difference scheme described in Bowers & Wilson (1991) and Thoul & Weinberg (1995). Shocks are treated with an artificial tensor viscosity (Tscharnutter & Winkler 1979). The number of mass shells is $N_b = 300$ for baryonic gas and $N_d = 10\,000$ for dark matter. Our code reproduces accurately the similarity solutions for the adiabatic accretion of collisional gas and the pressureless collapse around a point-mass perturbation (Bertschinger 1985). We have also checked that our results are essentially unchanged when the shell numbers are doubled or halved.

At each time-step of the simulation, we solve self-consistently the radiative transfer equation, chemical reactions, and energy equation in the following three steps. Repeating these procedures, the radiation field and the internal state of the gas are determined iteratively until the abundance of each species and the internal energy in each mesh converge within an accuracy of 0.1 per cent.

First, the direction/frequency-dependent radiative transfer is worked out for ionizing photons with energies $h\nu \geq 13.6\text{ eV}$, with the method devised by Tajiri & Umemura (1998), in which both absorption and emission by hydrogen are explicitly taken into account. At each radial point, angular integration of the transfer equation is done over at least 20 bins in $\theta = 0 - \pi$, where θ is the angle between the light ray and the radial direction. This is achieved by handling 400–1000 impact parameters for light rays. Self-shielding of H_2 against the LW photons (11.2–13.6 eV) is evaluated from the self-shielding function of Draine & Bertoldi (1996), considering the direction dependence of the H_2 column density as in Kepner et al. (1997). The gas is assumed to be optically thin against the photons with $h\nu < 11.2\text{ eV}$, which only contribute to destructions of H^- and H_2^+ .

Secondly, non-equilibrium chemical reactions are solved in each mesh for the species e , H , H^+ , H^- , H_2 , H_2^+ . Hydrogen molecules form mainly via the creation of the intermediates H^- and H_2^+ (eqs 1.1–1.4 of Shapiro & Kang 1987). We neglect helium for the following reasons: (i) it only changes the ionization degree of the gas up to ~ 10 per cent (Osterbrock 1989; Susa & Umemura 2000a); (ii) helium line cooling is unimportant at the typical temperatures ($T \lesssim 10^4\text{ K}$) of the objects presently studied; and (iii) photoionization heating of helium does not alter our main results as discussed in Section 3.1. Unless stated explicitly, reaction rates are taken from the recent compilation of Galli & Palla (1998). The coefficients for photoionization of H and photodissociation of H_2 are computed from the results of the radiative transfer mentioned above. Photodetachment of H^- and photodissociation of H_2^+ are also taken into account using the cross-sections given in Tegmark

et al. (1997) and Stancil (1994) for the photons with $h\nu \geq 0.74$ eV and $h\nu \geq 0.062$ eV, respectively. These two processes, particularly the former, can suppress H_2 formation by destroying its intermediates.

Finally, the energy equation is solved including UV heating and radiative cooling resulting from collisional ionization, collisional excitation, recombination, thermal bremsstrahlung, Compton scattering with the cosmic microwave background (CMB) radiation, and rotational-vibrational excitation of H_2 . The UV heating rate is obtained directly from the results of the radiative transfer. The atomic cooling rates are taken from Fukugita & Kawasaki (1994) and molecular cooling rates from Galli & Palla (1998).

For comparison with previous approaches, we also perform simpler calculations in the following two ways. One assumes at each time-step an optically thin medium and ionization equilibrium among e, H and H^+ , neglecting H_2 , H^- and H_2^+ . The other solves radiative transfer of ionizing photons, but neglects H_2 , H^- and H_2^+ . The latter corresponds to the analysis of Paper II. Hereafter we refer to the former as the ‘optically thin calculation’, the latter as the ‘no H_2 calculation’, and the one described in the previous paragraphs as the ‘full calculation’. Unless otherwise stated, the full calculation is adopted.

2.2 External UVB

The external UVB is assumed to be isotropic and to have either a power-law or blackbody spectrum:

$$J_{\nu}^{\text{ext}} \propto \begin{cases} \nu^{-\alpha}, \\ \nu^3, \end{cases} \quad (1)$$

$$\frac{1}{\exp(h\nu/k_B T_{\text{eff}}) - 1},$$

where k_B is the Boltzmann constant. We adopt the spectral index $\alpha = 1$ and the effective temperature $T_{\text{eff}} = 10^4$ K, to mimic the spectra of QSOs and stars, respectively. The above spectrum is normalized to give the intensity J_{21} , in units of $10^{-21} \text{ erg s}^{-1} \text{ cm}^{-2} \text{ sr}^{-1} \text{ Hz}^{-1}$, at the Lyman limit of hydrogen ($h\nu = 13.6$ eV).

Fig. 1 illustrates the model spectra described above with $J_{21} = 1$. Also shown for reference are those with $\alpha = 5$ and $T_{\text{eff}} = 5 \times 10^4$ K. In the present analyses, the ratio between the fluxes below and above the Lyman limit is a key parameter to control the radiative feedback on the gas evolution (e.g. Ciardi, Ferrara & Abel 2000a). To help quantitative comparisons among different spectral shapes, we list in Table 1 the photon-number-weighted average intensities of these spectra:

$$\langle J \rangle = \frac{\int J_{\nu}^{\text{ext}} / h\nu d\nu}{\int 1/h\nu d\nu} \times \frac{1}{10^{-21} \text{ erg s}^{-1} \text{ cm}^{-2} \text{ sr}^{-1} \text{ Hz}^{-1}}, \quad (2)$$

where the average is taken over the energies relevant for destruction of both H_2 and H^- (0.74–13.6 eV), dissociation of only H_2 (11.2–13.6 eV), and ionization of H (13.6– 10^4 eV). Notice that for a given value of J_{21} the spectrum with $T_{\text{eff}} = 10^4$ K has considerably less ionizing (>13.6 eV) photons and more H_2 and H^- destroying photons (<13.6 eV) than the one with $\alpha = 1$.

Observations of the proximity effect in the Ly α forest suggest $J_{21} = 10^{\pm 0.5}$ at redshift $z = 1.7$ –4.1 (Bajtlik et al. 1988; Bechtold 1994; Giallongo et al. 1996; Cooke, Espey & Carswell 1997), but its value is still highly uncertain at other redshifts. Recent CMB power spectrum measurement by MAXIMA has been used to constrain the redshift of reionization to be $z \approx 8$ at the 2σ confidence level (Schmalzing, Sommer-Larsen & Götz 2000). In

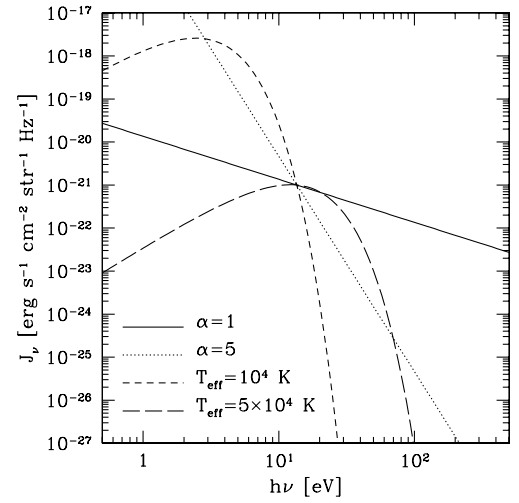


Figure 1. Model spectra of the external UVB with $\alpha = 1$ (solid), $\alpha = 5$ (dotted), $T_{\text{eff}} = 10^4$ K (short dashed), and $T_{\text{eff}} = 5 \times 10^4$ K (long dashed), all normalized to give $J_{21} = 1$.

Table 1. Average intensities $\langle J \rangle$ defined by equation (2) in specific energy ranges. All spectra are normalized to give $J_{21} = 1$.

spectrum	0.74–13.6 eV	11.2–13.6 eV	13.6– 10^4 eV
$\alpha = 1$	6.0	1.1	0.15
$\alpha = 5$	1.4×10^5	1.7	3.0×10^{-2}
$T_{\text{eff}} = 10^4$ K	1.3×10^3	3.8	1.1×10^{-2}
$T_{\text{eff}} = 5 \times 10^4$ K	0.39	1.0	8.6×10^{-2}

this paper, we fiducially fix the onset of the UVB at $z_{\text{UV}} = 20$ and consider at $z \leq z_{\text{UV}}$ constant J_{21} of an arbitrary value. To take into account uncertainties in the reionization history, we also examine some cases with $z_{\text{UV}} = 10$ and 50, and evolving J_{21} of the form

$$J_{21} = \begin{cases} \exp[-(z-5)], & 5 \leq z \leq 20, \\ 1, & 3 \leq z \leq 5, \\ \left(\frac{1+z}{4}\right)^4, & 0 \leq z \leq 3, \end{cases} \quad (3)$$

where the evolution at $z > 5$ is roughly consistent with recent models of reionization of the universe (Ciardi et al 2000b; Umemura, Nakamoto & Susa 2000).

2.3 Initial and boundary conditions

Initial and boundary conditions are similar to those in Sections 2.3 and 2.4 of Paper I. In the following, we give their brief summary and state any modifications and additions.

We start the simulations when the overdensity of a cloud is still in the linear regime. The initial overdensity profile for both baryon and dark matter is $\delta_i(r) = \delta_i(0) \sin(kr)/kr$, where k is the comoving wavenumber, and the central overdensity $\delta_i(0)$ is fixed at 0.2. Only the growing mode is considered. The outer boundary is taken at the first minimum of $\delta_i(r)$, i.e. $kr = 4.4934$, within which the volume-averaged overdensity $\bar{\delta}_i(<r)$ vanishes. The characteristic mass of a cloud M_{cloud} is defined as the baryon mass enclosed within the first zero of $\delta_i(r)$, i.e., $kr = \pi$, which is 0.363 of the total baryon mass (Haiman, Thoul & Loeb 1996a). We define the central collapse redshift z_{c0} and the cloud collapse redshift z_c , respectively, as epochs at which the innermost gas shell and the shell enclosing

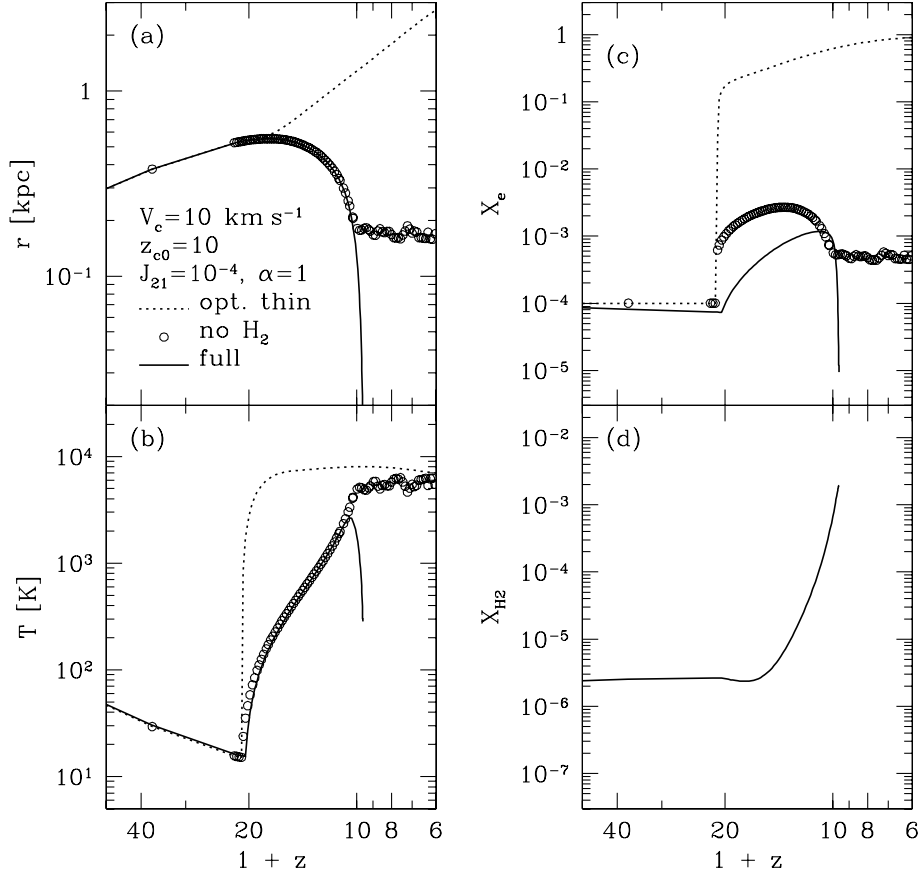


Figure 2. Time evolution of (a) radius, (b) temperature, (c) electron fraction, and (d) H_2 fraction, of the central gas shell of a low-mass object with $V_c = 10 \text{ km s}^{-1}$ and $z_{c0} = 10$ ($z_c = 3$), comparing different treatments of radiative processes. Lines and symbols indicate results of the optically thin (dotted line), no H_2 (circles), and full (solid line) calculations with $J_{21} = 10^{-4}$ and $\alpha = 1$.

M_{cloud} would collapse to the centre in the absence of thermal pressure. These two redshifts are related by $1 + z_{c0} \approx 2.7(1 + z_c)$ (strictly speaking, this relation is correct in the Einstein–de Sitter universe, but it still gives a reasonable approximation in the present case at $z_c \gtrsim 1$). We will often characterize a cloud by its circular velocity V_c and virial temperature T_{vir} , defined in terms of z_c and M_{cloud} as

$$V_c = 15.9 \left(\frac{M_{\text{cloud}} \Omega_0 / \Omega_b}{10^9 h_{100}^{-1} M_\odot} \right)^{1/3} \times \left\{ \frac{\Delta_c(z_c)}{18\pi^2} \right\}^{1/6} (1 + z_c)^{1/2} \text{ km s}^{-1}, \quad (4)$$

$$T_{\text{vir}} = 9.09 \times 10^3 \left(\frac{\mu}{0.59} \right) \left(\frac{M_{\text{cloud}} \Omega_0 / \Omega_b}{10^9 h_{100}^{-1} M_\odot} \right)^{2/3} \times \left\{ \frac{\Delta_c(z_c)}{18\pi^2} \right\}^{1/3} (1 + z_c) \text{ K}, \quad (5)$$

where μ is the mean molecular weight in units of the proton mass m_p , and $\Delta_c(z_c)$ is the mean overdensity of a virialized object predicted from the spherical infall model (Peebles 1980; Kitayama & Suto 1996). Using circular velocity or virial temperature to denote the size of an object, we can minimize the dependences of our simulation results on assumed cosmological parameters.

The initial abundance of each species is taken to be its cosmological post-recombination value (e.g. Galli & Palla 1998), i.e. $X_e = 10^{-4}$, $X_{\text{H}^-} = 10^{-12}$, $X_{\text{H}_2} = 10^{-6}$ and $X_{\text{H}_2^+} = 10^{-13}$,

where $X_i \equiv n_i/n_{\text{H}}$ is the fraction of the species i with respect to the total number of hydrogen atoms. Our results are insensitive to the precise values of initial abundances. In the optically thin and no H_2 calculations, $X_e = 10^{-4}$ is assumed before the gas is exposed to the UVB or experiences shocks.

In this paper, we mainly focus on the evolution of the central gas of a cloud until it reaches the rotation radius specified by the dimensionless spin parameter at turn-around λ_{ta} :

$$r_{\text{rot}} = 0.03 \left(\frac{\Omega_b / \Omega_0}{0.17} \right)^{-1} \left(\frac{\lambda_{\text{ta}}}{0.05} \right)^2 r_{\text{ta}}, \quad (6)$$

where r_{ta} is the turnaround radius of the shell, and we adopt a median for the spin parameter, $\lambda_{\text{ta}} = 0.05$ (Efstathiou & Jones 1979; Barns & Efstathiou 1987; Warren et al. 1992). The above radius defines the scale below which the gas is supposed to attain rotational support and the approximation of spherical symmetry breaks down. The overdensity of the gas exceeds $\sim 10^5$ when it reaches this radius. The simulation is halted when the innermost gas shell has fallen below this radius and is regarded as ‘collapsed’. On the other hand, a dark matter shell falling to the centre is rebounded at the radius r_{rot} of the innermost gas shell, to mimic shell crossings.

At the outer boundary, we assume that the gas is in pressure equilibrium, i.e. the pressure outside the cloud P_{out} is equal to that of the outermost gas shell. This is different from the free boundary condition ($P_{\text{out}} = 0$) adopted in Papers I and II. While the inner structure of a simulated cloud is hardly affected by this difference,

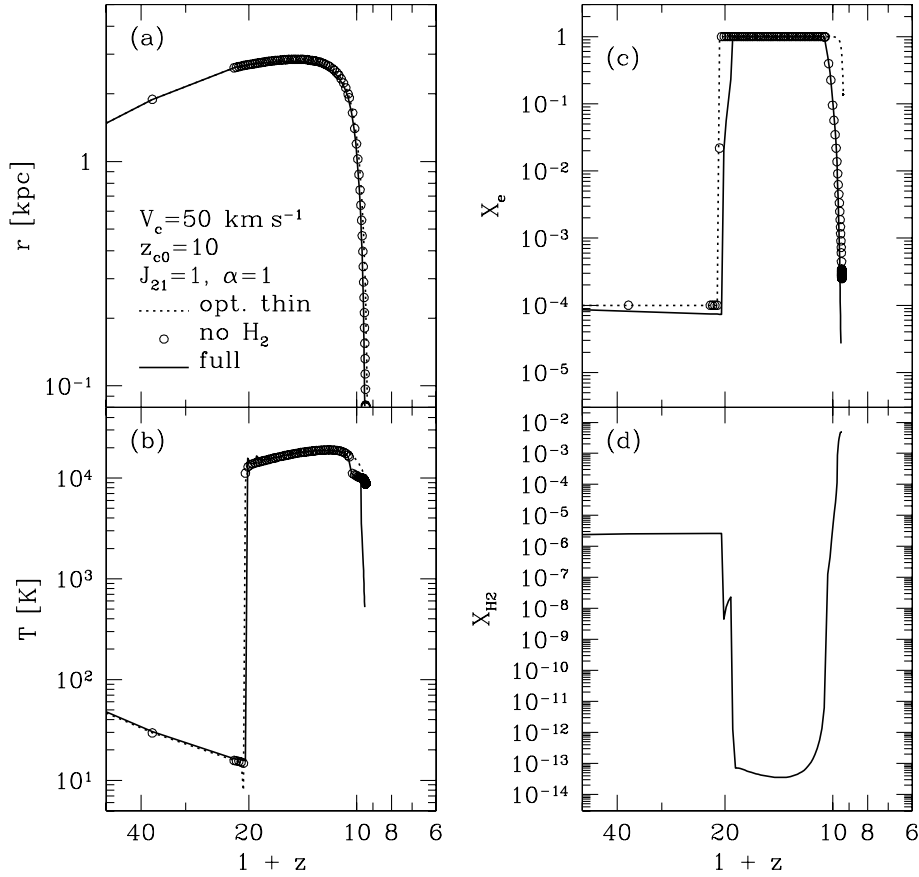


Figure 3. Same as Fig. 2, except for showing a high-mass collapse with $V_c = 50 \text{ km s}^{-1}$ in the UVB with $J_{21} = 1$ and $\alpha = 1$.

we adopt the former in this paper so that the cloud envelope continues to follow the Hubble expansion throughout its evolution.

3 RESULTS

3.1 Significance of radiative transfer and H_2 formation

The results of the full calculations are first compared with those of previous approaches, to illustrate the significance of incorporating radiative transfer and H_2 formation in our analyses. The most noticeable changes are in the evolution of a low-mass object with $T_{\text{vir}} < 10^4 \text{ K}$. Fig. 2 shows the time evolution of the central part of a cloud with $z_{c0} = 10$ ($z_c = 3$) and $V_c = 10 \text{ km s}^{-1}$, corresponding to $T_{\text{vir}} = 4 \times 10^3 \text{ K}$. Both the dynamics and the thermal state are shown to change completely under different treatments of the radiative processes. In the optically thin calculation, the cloud is photoionized to the centre and evaporated promptly by a little radiation with $J_{21} = 10^{-4}$ and $\alpha = 1$. In the no H_2 calculation, the external radiation is attenuated by absorption, but contraction of the gas is halted by thermal pressure as it lacks coolant at $T < 10^4 \text{ K}$. In the full calculation, on the other hand, the cloud centre is kept self-shielded against the UVB and H_2 molecules in excess of $X_{H_2} = 10^{-3}$ are produced, allowing the gas to collapse and cool efficiently to $\sim 10^2 \text{ K}$. Details of the H_2 formation and destruction processes in the UVB will be discussed in Section 3.2.

For a high-mass object well above the scale $T_{\text{vir}} = 10^4 \text{ K}$, in contrast, radiative transfer and H_2 formation appear to have smaller impacts as far as the dynamics is concerned. Fig. 3 shows that such a cloud can collapse even in a stronger UV field with $J_{21} = 1$ and

$\alpha = 1$, regardless of treatments of radiative processes. This is because gravitational potential of the cloud is much greater than thermal energy attained by photoionization ($T \sim 10^4 \text{ K}$) and atomic cooling is efficient enough to enable the collapse.

Nevertheless, the final thermal state of the gas is still modified to a great extent in a high-mass collapse, as indicated by the differences in the temperature and electron fraction at the collapse in Fig. 3. To see this point more clearly, Fig. 4 compares the internal structure of the same objects at the collapse of the central gas. The density profile commonly shows that the central gas is undergoing run-away collapse (panel a), as it cools efficiently and contracts nearly at the free-fall rate under the dark matter potential. The radiative transfer effects, however, produce a self-shielded neutral region at $r \lesssim 2 \text{ kpc}$ (panel b), whereas X_{H_1} is simply determined by ionization equilibrium with uniform radiation in the optically thin case. The gas well inside this neutral region can cool down to $\sim 10^2 \text{ K}$ once H_2 cooling is taken into account (panel c). In the absence of H_2 molecules, the gas can cool only to $\sim 10^4 \text{ K}$ by atomic cooling. Rapid increase of density resulting from run-away collapse is in fact essential for self-shielding and H_2 cooling, as will be discussed thoroughly in the forthcoming sections.

To further corroborate the above results, Fig. 5 shows more detailed structures in the full calculation. While H_2 molecules are destroyed in the ionized outer envelope, they form efficiently in the self-shielded central region (panel a). Roughly speaking, the gas becomes optically-thick against ionizing ($> 13.6 \text{ eV}$) photons at $N_{H_1} \gtrsim 10^{17} \text{ cm}^{-2}$ and the LW (11.2–13.6 eV) photons at $N_{H_2} \gtrsim 10^{14} \text{ cm}^{-2}$, where N_{H_1} and N_{H_2} are respectively the H_1 and H_2 column densities measured from the outer boundary. Both

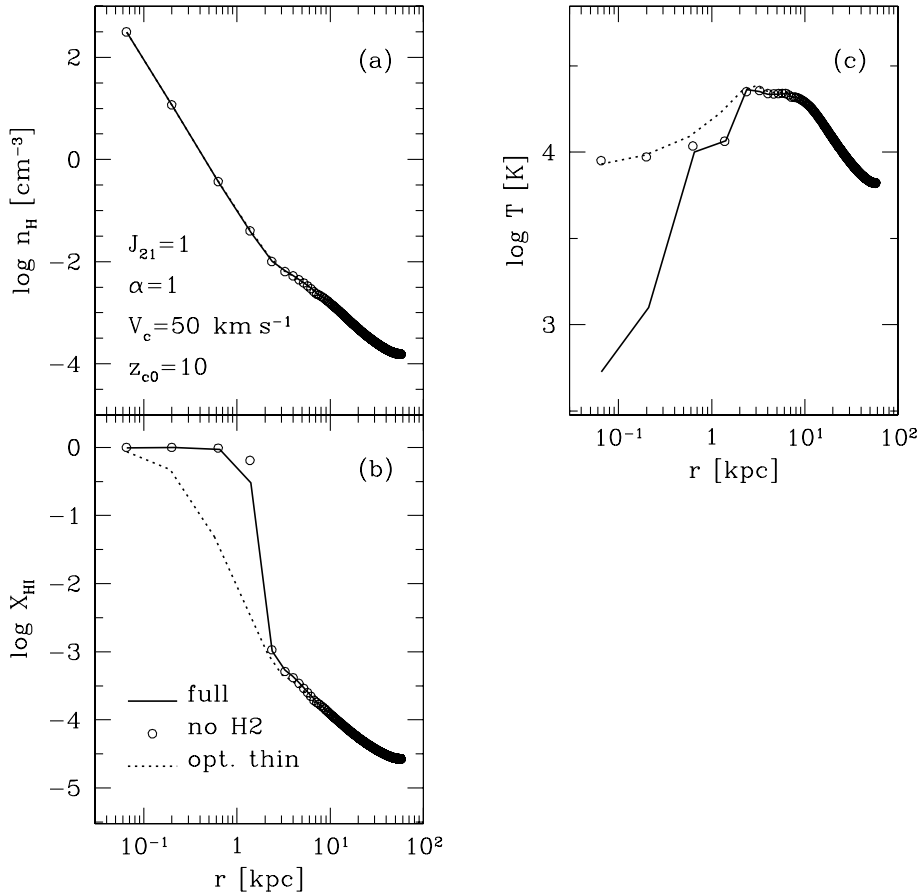


Figure 4. Radial profiles at the collapse of the cloud centre, comparing the optically thin (dotted line), no H_2 (circles), and full (solid line) calculations: (a) total hydrogen density, (b) H I fraction, and (c) temperature. $J_{21} = 1$, $\alpha = 1$, $V_c = 50 \text{ km s}^{-1}$ and $z_{c0} = 10$ ($z_c = 3$) are adopted.

of these conditions are amply satisfied at $r \lesssim 1 \text{ kpc}$ (panel b). The UV heating rate is reduced significantly in this optically thick region (panel c). Photons emitted in the cloud interior contribute at most ~ 10 per cent to the total heating rate for the $\alpha = 1$ spectrum, though their contribution can be much larger for a softer spectrum (Tajiri & Umemura 2001). Cooling to temperatures below 10^4 K is possible once H_2 cooling overtakes UV heating. At $T \lesssim 10^4 \text{ K}$ ($r \lesssim 0.8 \text{ kpc}$), the time-scale of H_2 formation becomes shorter than that of destruction as recombination lags behind the temperature decrease (Kang & Shapiro 1992; Corbelli, Galli & Palla 1997), and chemical reactions are out of equilibrium (panel d). The cooling time-scale, however, becomes even shorter as temperature drops, and X_{H_2} is frozen out at $\sim 10^{-3}$ at the cloud centre. This abundance is comparable to that achieved commonly in a metal-deficient post-shock layer in the absence of radiation (Shapiro & Kang 1987; Ferrara 1998; Susa et al. 1998).

If helium is further incorporated into the present calculations, the largest impact will be via heating by photons with $h\nu \gtrsim 24.6 \text{ eV}$. For given UV intensity J_{21} , H I number density $n_{\text{H I}}$, and H I column density $N_{\text{H I}}$, the heating rate will be enhanced by the addition of helium, in the case of $\alpha = 1$, as

$$\frac{\mathcal{H}(\text{H} + \text{He})}{\mathcal{H}(\text{H})} \approx \begin{cases} 1 + 0.19 \left(\frac{n_{\text{He I}}/n_{\text{H I}}}{0.08} \right), & \text{optically thin limit,} \\ 1.46 \left(\frac{n_{\text{He I}}/n_{\text{H I}}}{N_{\text{He I}}/N_{\text{H I}}} \right), & \text{optically thick limit,} \end{cases} \quad (7)$$

where $\mathcal{H}(\text{H} + \text{He})$ is the total heating rate in units of $\text{erg s}^{-1} \text{ cm}^{-3}$ of both H and He , and $\mathcal{H}(\text{H})$ is that of the pure hydrogen gas. These rates are computed as in the Appendix of Paper I, and are in good agreement with more rigorous treatment. Equation (7) indicates that the total heating rate tends to increase by ~ 20 – 50 per cent once helium with the primordial abundance (~ 8 per cent by number) is taken into account. This is much smaller than the overall variations in the heating and cooling rates in a cloud shown in Fig. 5(c). In fact, we have checked that an additional heat input of 50 per cent does not considerably alter either the time evolutions in Figs 2 and 3 or the internal structures in Figs 4 and 5. Though temperature of the diffuse outer envelope can increase by as much as a factor of 2 by helium heating (Abel & Haehnelt 1999), the evolution of the central high-density region, in which our main interests reside, is little influenced. Helium heating will be of less importance for softer spectra. Hence we neglect helium in our analyses.

In summary, the above results justify our present approach and confirm the importance of including radiative transfer of UV photons, H_2 formation/destruction and hydrodynamics, in studying the development of Population III objects in the UVB.

3.2 Dynamical and thermal evolution

The evolution of UV irradiated clouds are studied in more detail in the following. Fig. 6 displays how the time evolution of a low-mass object ($V_c = 10 \text{ km s}^{-1}$) depends on the radiation intensity. In the absence of the UVB ($J_{21} = 0$), the cloud decoupled from the Hubble expansion is first shock-heated and then cools radiatively.

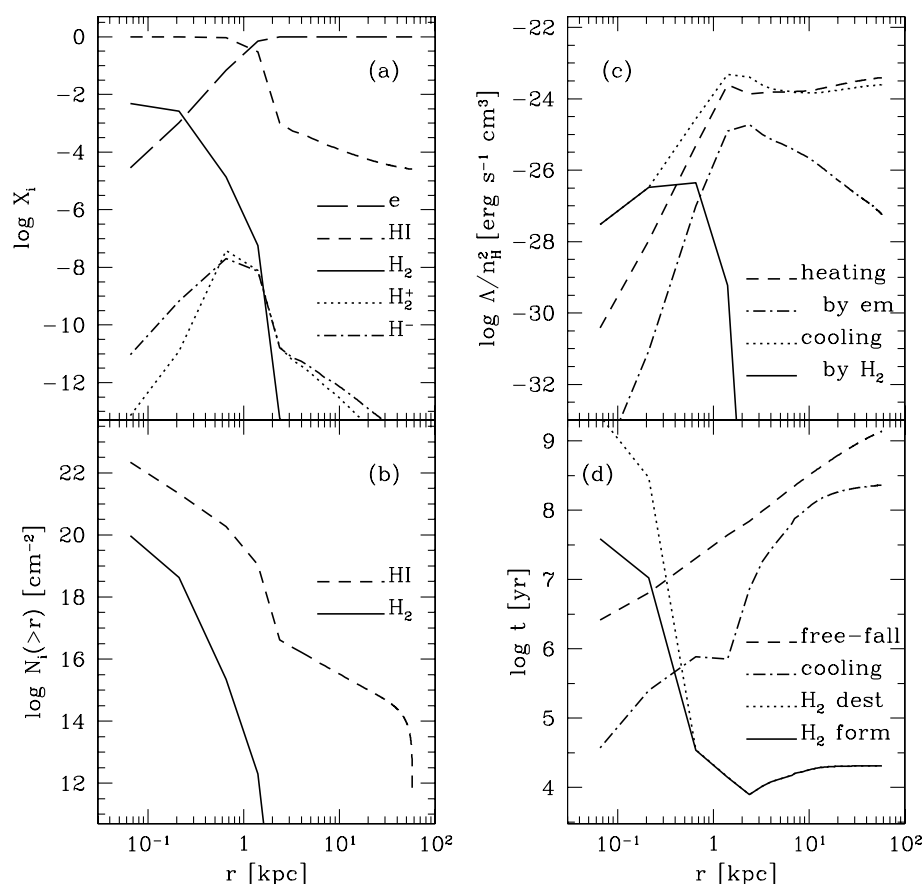


Figure 5. Detailed radial profiles in the same full calculation as in Fig. 4: (a) fractions of e (long-dashed), $H\text{I}$ (short-dashed), H_2 (solid), H_2^+ (dotted), and H^- (dot-dashed), (b) column densities of $H\text{I}$ (dashed) and H_2 (solid) measured from the outer boundary, (c) rates of total UV heating (dashed), UV heating by emitted photons (dot-dashed), total cooling (dotted), and H_2 cooling (solid), and (d) time-scales of free-fall (dashed), cooling (dot-dashed), H_2 destruction (dotted), and H_2 formation (solid).

At $J_{21} = 10^{-2}$, in contrast, the gas is photoionized and evaporated even if radiative transfer is taken into account. Once the gas is photoionized and heated, H_2 molecules are destroyed by a large amount. At lower intensity ($J_{21} = 10^{-4}$), as was also shown in Fig. 2, the cloud can collapse and cool down by H_2 . At even weaker intensity ($J_{21} = 10^{-6}$), the radiation is attenuated almost completely and the evolution resembles that in the no UV case. Note that the H_2 fraction increases after the onset of the UVB at $J_{21} = 10^{-4}$, compared with the no UV case. This is indeed the case in which the formation of H_2 via H^- and H_2^+ is promoted by an enhanced ionized fraction in a weakly photoionized medium (Haiman et al. 1996b).

Fig. 7 illustrates that the shape of the radiation spectrum also influences greatly the thermal and dynamical evolution. Compared to the $\alpha = 1$ case, the blackbody spectrum with $T_{\text{eff}} = 10^4$ K is softer and has much fewer ionizing photons with energies above 13.6 eV (see Fig. 1 and Table 1). For the same values of J_{21} as in Fig. 6, the blackbody UVB therefore has weaker impacts on the evolution of radius, temperature and the ionization degree. On the other hand, H_2 molecules are destroyed by a larger amount at the onset of the UVB, because a greater number of photons with energies below 13.6 eV are available to destroy H_2 and its intermediates, H^- and H_2^+ . Nevertheless, as the gas contracts, it becomes optically thick against the LW photons and the final H_2 fraction of $X_{H_2} \sim 10^{-3}$ is still achieved.

For a high mass object well above the scale $T_{\text{vir}} = 10^4$ K, the collapse is hardly suppressed even under the strong UVB, but its

thermal evolution remains sensitive to the UVB. As shown in Fig. 8, for $J_{21} \geq 1$ and $\alpha = 1$, the gas is promptly heated to $\sim 10^4$ K and H_2 molecules are destroyed mainly via collisions with H^+ . At $J_{21} = 10^{-2}$, on the other hand, the H_2 abundance is enhanced compared with the no UV case by an increased degree of ionization, as already mentioned. In either case, the H_2 fraction at the collapse again exceeds $X_{H_2} \sim 10^{-3}$.

To illustrate more clearly how self-shielding and radiative cooling operate in a collapsing cloud, we plot in Figs 9 and 10 the temperature and fractions of $H\text{I}$ and H_2 at the cloud centre as a function of its density. As the gas contracts and density rises, its state changes rather suddenly from the hot ($T > 10^4$ K) ionized ‘ $H\text{II}$ phase’, to the warm ($T \sim 10^4$ K) neutral ‘ $H\text{I}$ phase’, and the cold ($T < 10^4$ K) neutral ‘ H_2 phase’. Such transitions are analogous to those pointed out by Kepner et al. (1997), except that they are induced here by the dynamical contraction of the gas itself rather than the decline of the external UV intensity. The transition from the $H\text{II}$ phase to the $H\text{I}$ one takes place when the cloud becomes optically thick against ionizing photons. The gas finally enters the H_2 phase once the cooling time-scale becomes shorter than the other relevant time-scales, such as those of free-fall and H_2 formation/destruction. These figures confirm that X_{H_2} tends to converge to $\sim 10^{-3}$ after the H_2 phase is achieved.

Figs 9 and 10 further indicate that quantitative details of the transitions among the above phases depend sensitively on the intensity and spectrum of the UVB. To examine this more directly, we plot in Fig. 11 the critical densities for $H\text{I}$ shielding $n_{\text{H}}^{\text{cr}}(H\text{I})$ and

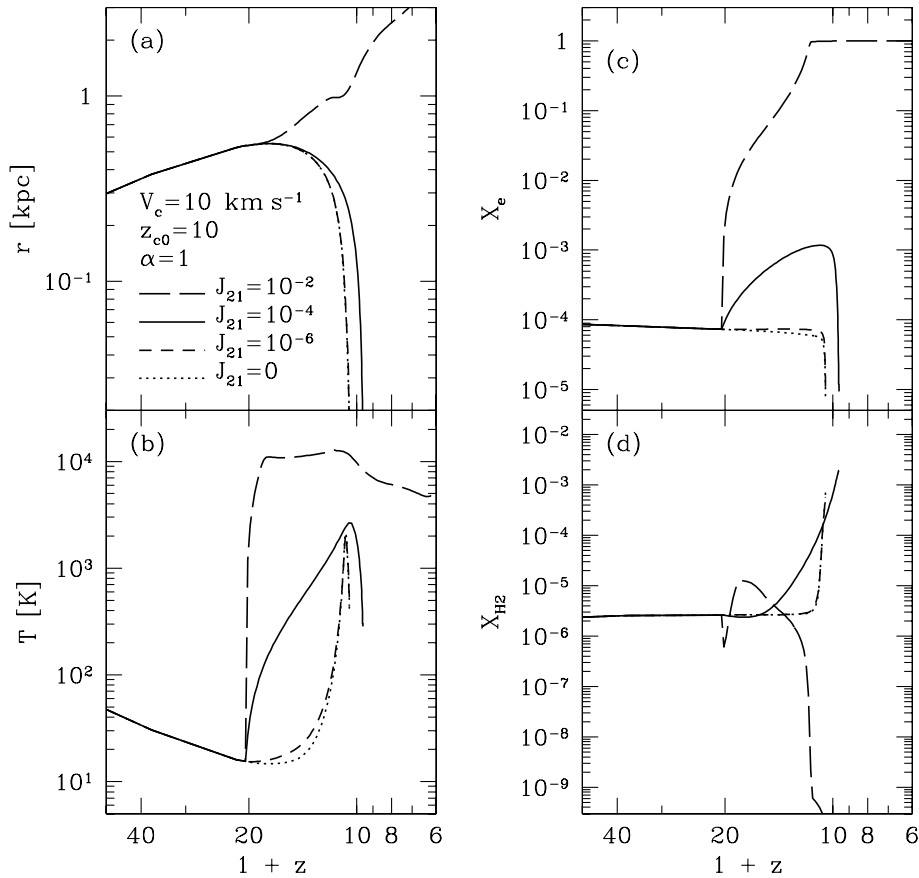


Figure 6. Same as Fig. 2, except for comparing different values of J_{21} in the case of $\alpha = 1$. Lines indicate the results with $J_{21} = 10^{-2}$ (long dashed), 10^{-4} (solid), 10^{-6} (short dashed), and 0 (dotted). The results of $J_{21} = 10^{-6}$ and 0 closely overlap each other.

H_2 cooling $n_H^{\text{cr}}(H_2)$, defined as those at which the central $H\text{I}$ fraction exceeds 0.5 and the temperature falls below 5000 K, respectively. In what follows, we regard the gas as in the $H\text{II}$, $H\text{I}$, and H_2 phases, if the density is in the range $n_H < n_H^{\text{cr}}(H\text{I})$, $n_H^{\text{cr}}(H\text{I}) < n_H < n_H^{\text{cr}}(H_2)$, and $n_H > n_H^{\text{cr}}(H_2)$ respectively. Though Fig. 11 is plotted for particular choices of V_c and z_c , basic features are similar in other cases. A possible change is that for smaller masses and large J_{21} the collapse is completely prohibited (see Fig. 12) and the critical densities simply disappear.

Fig. 11 shows that $n_H^{\text{cr}}(H\text{I})$ increases with J_{21} for a given spectral shape, i.e., the higher density is required to shield the stronger ionizing flux. At small J_{21} , $n_H^{\text{cr}}(H\text{I})$ falls below the turnaround density, indicating that photoionization is kept attenuated throughout the cloud evolution. This feature is also apparent in Figs 9 and 10, in which $X_{H\text{I}}$ is kept high at weak UV intensities. Compared with the $\alpha = 1$ case, the $T_{\text{eff}} = 10^4$ K spectrum yields lower values of $n_H^{\text{cr}}(H\text{I})$, because there are fewer ionizing (>13.6 eV) photons for a given J_{21} .

On the other hand, $n_H^{\text{cr}}(H_2)$ behaves in a more complex manner, depending on the spectral shape. For $\alpha = 1$, it is not a monotonic function of J_{21} , but has a minimum at moderate intensities $J_{21} \sim 10^{-3}$ – 10^{-2} . Formation of H_2 molecules is enhanced maximally at these intensities. At weaker intensities $J_{21} \lesssim 10^{-4}$ the result almost coincides with that of the no UV case, whereas at stronger intensities $J_{21} \gtrsim 10^{-1}$ H_2 formation is suppressed to higher densities. For $T_{\text{eff}} = 10^4$ K, in contrast, a greater fraction of photons below 13.6 eV is present to suppress H_2 formation. The threshold $n_H^{\text{cr}}(H_2)$ is therefore higher than that of $\alpha = 1$ for a given J_{21} . This is the reason why the convergence of X_{H_2} is rather slow in

Fig. 10. In either case, Fig. 11 assures that the H_2 phase is realized at the centre of a contracting cloud before it is rotationally supported, as long as J_{21} is not far above the level $J_{21} \sim 1$ observed at $z \sim 3$.

The above critical densities $n_H^{\text{cr}}(H\text{I})$ and $n_H^{\text{cr}}(H_2)$ at $J_{21} \gtrsim 1$ with $\alpha = 1$ are in rough agreement with analytical estimations by Tajiri & Umemura (2001) for an isothermal sphere; $n_H^{\text{cr}}(H\text{I})$, $n_H^{\text{cr}}(H_2) \propto J_{21}^{2/3}$. This confirms, in the case of $\alpha = 1$, that $n_H^{\text{cr}}(H\text{I})$ is essentially the density at which the number of recombinations in a cloud exceeds that of ionizing photons. Similarly, $n_H^{\text{cr}}(H_2)$ at $J_{21} \gtrsim 1$ corresponds to the density at which the H_2 cooling rate overcomes the UV heating rate attenuated at the cloud centre. For a much softer spectrum ($T_{\text{eff}} = 10^4$ K), the deviations from such simplified estimations become larger, because of the greater significance of emitted photons and the LW photons.

3.3 Criteria for collapse and H_2 cooling

We have performed the simulations for a variety of parameters, such as the intensity and spectrum of the UVB, and the circular velocity and collapse redshift of a cloud. The results are summarized in the following.

Fig. 12 shows a $J_{21} - V_c$ diagram on collapse and cooling of a cloud with $z_{c0} = 10$ ($z_c = 3$). The final state of the central gas is classified into three categories: (i) it collapses and cools to $T < 5000$ K, i.e. the H_2 phase is realized; (ii) it collapses but does not cool to $T < 5000$ K; and (iii) it is prohibited to collapse within the present age of the Universe. Also plotted for reference is the relation $T_{\text{vir}} = T_{\text{eq}}^{\text{max}}$, where $T_{\text{eq}}^{\text{max}}$ is the maximum equilibrium

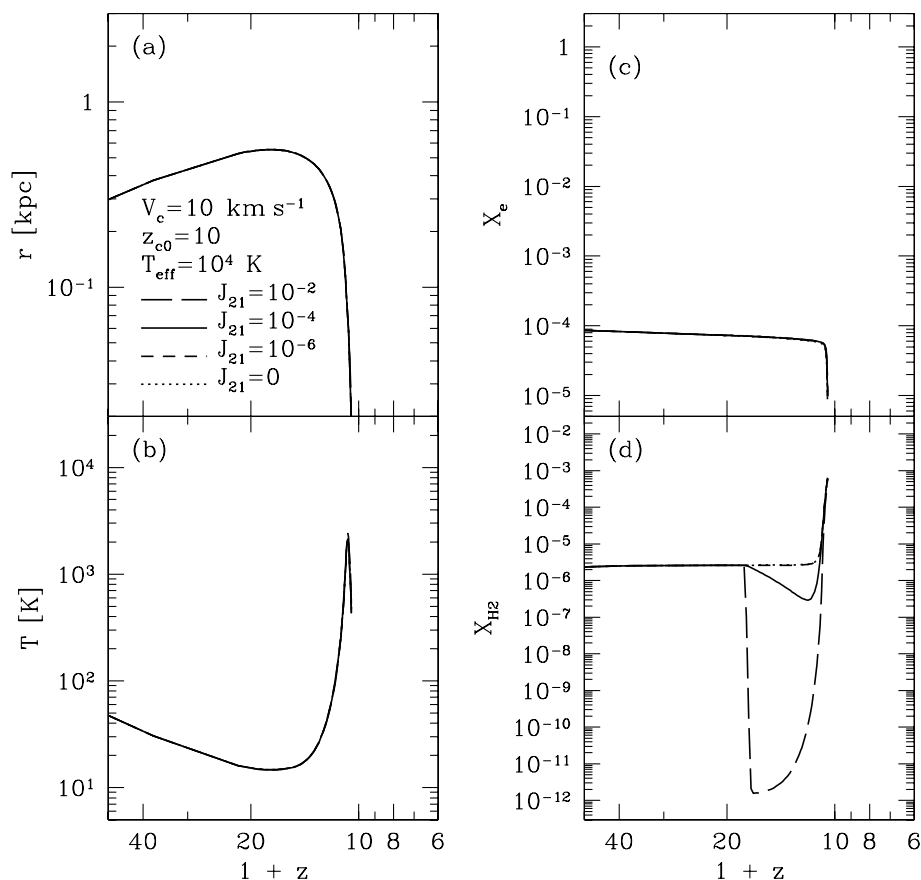


Figure 7. Same as Fig. 6, except for adopting a blackbody spectrum with $T_{\text{eff}} = 10^4$ K. In panels (a)–(c), all the lines overlap one another.

temperature defined semi-analytically in Section 3.3 of Paper II. This relation roughly corresponds to the Jeans condition at the maximum expansion of the central gas and provides a reasonable estimation for the collapse threshold in the optically thin limit.

The predictions of the full calculations are distinct from the optically thin results in two ways. One is that the collapse of low-mass objects with $T_{\text{vir}} < 10^4$ K ($V_c < 17$ km s $^{-1}$) is possible at small UV intensities. The other is that the central gas in collapsed clouds can cool efficiently to temperatures well below 10^4 K, as long as J_{21} is not far above the observed level $J_{21} \sim 1$. The suppression of H $_2$ cooling occurs at $J_{21} \gtrsim 10^4$ for $\alpha = 1$ and $J_{21} \gtrsim 10^2$ for $T_{\text{eff}} = 10^4$ K, mainly owing to photodetachment of H $^-$ as well as photodissociation of H $_2$. To quantify this effect, we indicate in Fig. 12 the average intensity of the external UVB defined by equation (2) at 0.74–13.6 eV. The suppression of H $_2$ cooling is shown to take place at $\langle J(0.74\text{--}13.6\text{ eV}) \rangle \gtrsim 5 \times 10^4$ in massive clouds for both spectra.

Given circular velocity and collapse redshift of a cloud, one can compute the critical radiation intensity for collapse and H $_2$ cooling. Fig. 13 exhibits, as a function of the central collapse redshift z_{c0} , the intensity above which H $_2$ cooling is prevented completely in a cloud, i.e. the final state of the central gas belongs to the category (ii) or (iii) defined above. The critical intensity is in general an increasing function of redshift, i.e. gas density. It also increases with circular velocity but converges at $V_c \gtrsim 50$ km s $^{-1}$ and $V_c \gtrsim 30$ km s $^{-1}$ for $\alpha = 1$ and $T_{\text{eff}} = 10^4$ K, respectively. The convergence takes place once photoheating no longer affects the cloud evolution and only photodestruction of H $_2$ and H $^-$ becomes important. The converged intensities therefore have nearly

identical average values below the Lyman limit $\langle J(0.74\text{--}13.6\text{ eV}) \rangle \sim 30(1 + z_{c0})^3$ for both spectra. Once converged, the critical intensities tend to drop slightly for larger V_c (panel b) because the electron fraction of the gas is lower in a cloud with higher hydrogen column densities.

To explore the possibilities of different epochs of reionization, we have added to Fig. 13 the results of runs with $z_{\text{UV}} = 10$ and 50. If z_{c0} is sufficiently close to z_{UV} , the central gas is already contracting when it is exposed to the UVB, and hence the stronger intensity is required to prevent collapse and cooling. The difference is greater for the harder spectrum and the smaller cloud mass, for which suppression of cooling is mainly via photoevaporation and depends highly on the initial dynamical state of the gas. For the softer spectrum and the larger cloud mass, on the other hand, the suppression is regulated to a greater extent by photodestruction of H $_2$ and H $^-$, and is less sensitive to the initial dynamical state. After all, Fig. 13 indicates that there is a greater chance for the gas to cool even in a cloud well below the scale $V_c = 30$ km s $^{-1}$ at high redshifts, provided that the intensity is comparable to or less than $J_{21} \sim 1$.

Alternatively, given a specific model on the evolution of the UVB, one can deduce the critical circular velocity or mass for collapse and cooling. Fig. 14 shows such quantities under which H $_2$ cooling is completely suppressed in an object with the cloud collapse epoch z_c . The UVB greatly prohibits cooling in clouds with $V_c \lesssim 30$ km s $^{-1}$ or $M_{\text{cloud}} \lesssim 10^9 M_\odot$ at low redshifts. The threshold values, however, depend highly on the time history and spectra of the UVB. For an evolutionary model given by equation (3), the critical mass drops by several orders of magnitude at $z_c \gtrsim 3$

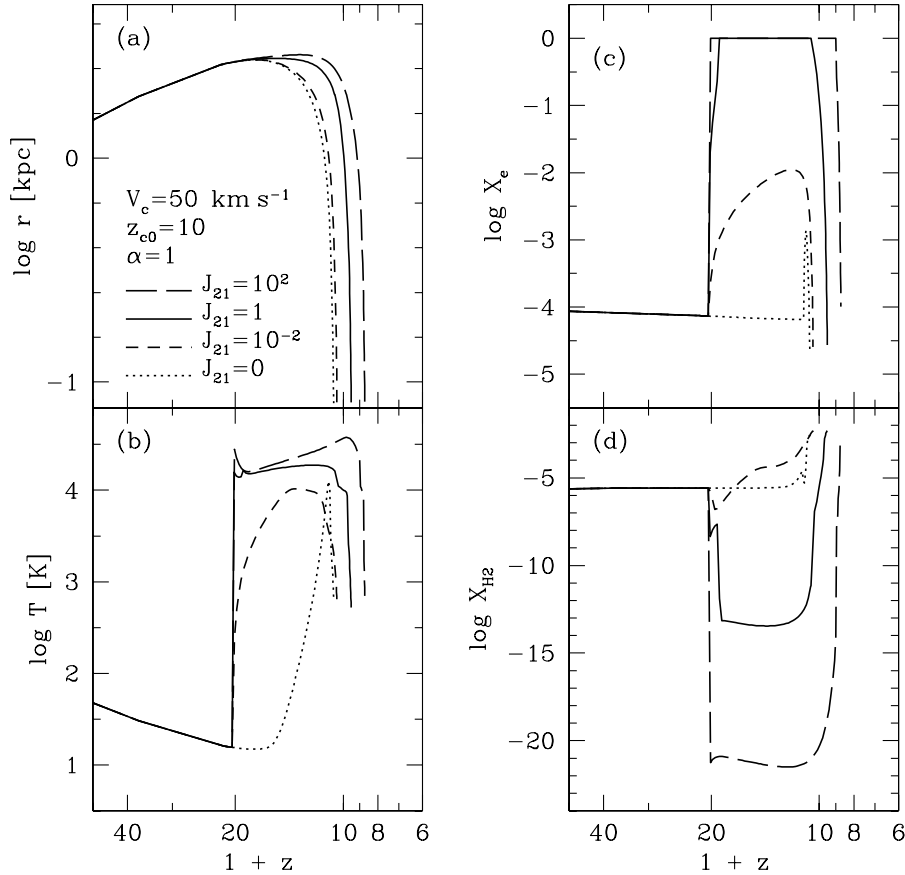


Figure 8. Same as Fig. 6, except for showing a high-mass collapse with $V_c = 50 \text{ km s}^{-1}$ in the UVB with $J_{21} = 10^2$ (long-dashed), 1 (solid), 10^{-2} (short-dashed), and 0 (dotted).

($z_{c0} \gtrsim 10$), enabling cooling in objects as small as $M_{\text{cloud}} \sim 10^6 M_\odot$.

Fig. 14(b) also exhibits the mass and collapse redshift of the 1, 2, 3σ density perturbations in a cold dark matter (CDM) model with $(\Omega_0, \lambda_0, h_{100}, \Omega_b, \sigma_8) = (0.3, 0.7, 0.7, 0.05, 1.0)$. This is a specific example of the most successful cosmological model which is consistent with a number of current observations (e.g. Wang et al. 2000). Fig. 14 shows that the UVB mainly suppresses collapse and cooling of $\lesssim 1\sigma$ objects with $M_{\text{cloud}} \lesssim 10^9 M_\odot$ in the Λ CDM model. It is rather difficult to suppress cooling in higher σ objects, unless the radiation intensity becomes much higher than the level observed at $z \sim 3$.

If different values of cosmological parameters are adopted, the collapse criterion in terms of circular velocity remains practically unchanged as long as $\Omega_b/\Omega_0 \ll 1$. Thus, the critical mass shown in Fig. 14(b) scales with cosmological parameters merely according to equation (4).

4 DISCUSSION

Our calculations predict that the formation of objects with $V_c \lesssim 30 \text{ km s}^{-1}$ is greatly suppressed by the UVB at low redshifts, whereas much smaller objects ($T_{\text{vir}} \lesssim 10^4 \text{ K}$, $V_c \lesssim 17 \text{ km s}^{-1}$) can collapse and cool at high redshifts ($z_c \gtrsim 3$, $z_{c0} \gtrsim 10$). This is mainly for three reasons: (i) intensity of the UVB tends to decline at high redshifts prior to complete reionization of the Universe; (ii) self-shielding of the gas is stronger at higher redshifts owing to higher gas density; and (iii) the gas density in Jeans-unstable

clouds rises rapidly along with runaway collapse, further promoting self-shielding and H_2 formation.

What are the fates of low-mass objects that are able to cool and collapse in the presence of the UVB? If the cooled gas can promptly turn into stars, they are likely to constitute ‘building blocks’ of present-day luminous structures. While such objects may be detected directly by future instruments such as *NGST*, they may also have links to observed subgalactic objects (e.g. Pascarella et al. 1996) or dwarf galaxies. In contrast, those prevented from collapsing by the UVB will become gravitationally unbound and spread into the intergalactic medium. They might contribute to Ly α absorption lines in the QSO spectra (e.g. Umemura & Ikeuchi 1984).

These speculations on the bifurcation of low-mass objects are illustrated schematically in Fig. 15. The critical baryonic mass in the case of evolving J_{21} (equation 3) with $\alpha = 1$ is used to distinguish the uncollapsed ‘expanding clouds’ from the others. Furthermore, we expect that the collapsed objects may be identified, mainly based on their distinct star formation histories, as at least two separate populations: the lower mass ($\lesssim 10^9 M_\odot$), higher σ ($\gtrsim 1\sigma$) systems and the higher mass, lower σ ones. The former population can be a plausible candidate of dwarf spheroidal/elliptical galaxies for the following reasons. First, star formation in these objects is expected to be active at redshifts higher than ~ 3 , consistent with the fact that the majority of local group dwarfs show a sharp decline in the star formation rate at some 10 Gyr ago (Mateo 1998; Gnedin 2000a). Secondly, their gravitational potential is compatible with small velocity

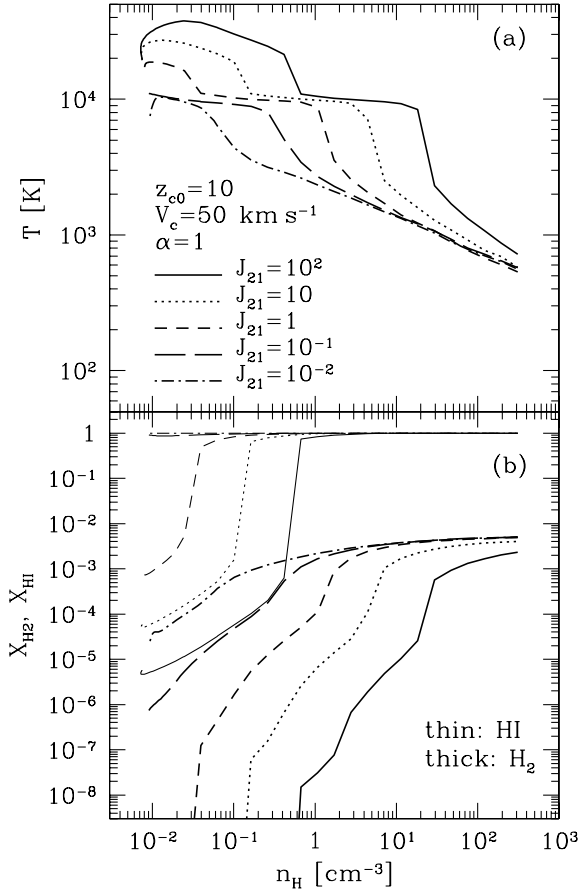


Figure 9. Evolution of (a) temperature, (b) X_{H_2} (thick lines) and X_{HI} (thin lines), versus gas density at the centre of a collapsing cloud with $V_c = 50$ km s⁻¹ and $z_{c0} = 10$ ($z_c = 3$) in the case of $\alpha = 1$. Lines indicate $J_{21} = 10^2$ (solid), 10 (dotted), 1 (short-dashed), 10⁻¹ (long-dashed), and 10⁻² (dot-dashed). For clarity, only the evolution at $z < 15$ is plotted.

dispersions ($\lesssim 10$ km s⁻¹) of local group dwarfs. Thirdly, they are apt to be dark matter dominated and metal-poor because the gas infall and star formation are suppressed particularly at the outer envelope. Fourthly, our simulations indicate that the central gas in these objects can cool efficiently by H₂ in the course of spherical contraction before reaching the rotation barrier. Galaxy formation is thus likely to proceed rapidly in a dissipationless manner and lead to the formation of spheroids rather than disks.

On the other hand, the latter population will exhibit signs of more recent star formation and contribute significantly to the global star formation rate of the Universe. The clustering of these low σ objects is expected to be rather weak. They might thus have been identified as a part of faint blue objects (e.g. Tyson 1988; Cowie et al. 1988; Ellis 1997) or star-forming dwarfs (e.g. Thuan & Martin 1981; Lee et al. 2000). This is in line with the idea proposed by Babul & Rees (1992) and extended by Babul & Ferguson (1996) and Kepner et al. (1997). One distinction is that the impacts of the decline of the UV intensity at low redshifts turn out to be modest. This is because the collapse is delayed by the kinetic energy of the gas attained during the peak of the UV intensity at $z \approx 3-5$ (although the threshold circular velocity does decrease with time, the threshold mass continues to rise by a factor $M/V_c^3 \sim [1 + z_c]^{-3/2}$).

The present spherical collapse simulations are mainly applicable to low-mass objects near the Jeans scale. Much larger objects, in

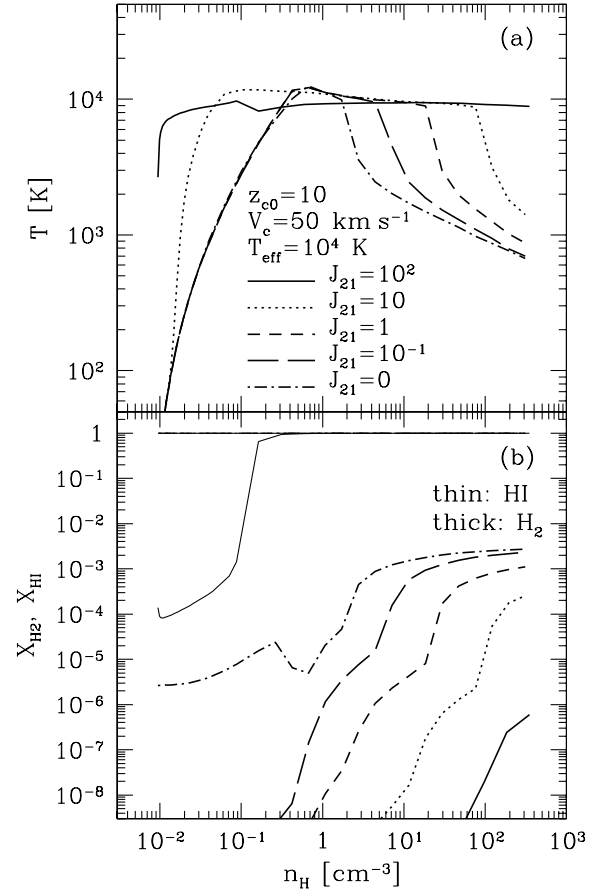


Figure 10. Same as Fig. 9, except that $T_{eff} = 10^4$ K is adopted and dot-dashed lines indicate $J_{21} = 0$. In panel (b), thin lines (X_{HI}) overlap one another for $J_{21} \leq 10$.

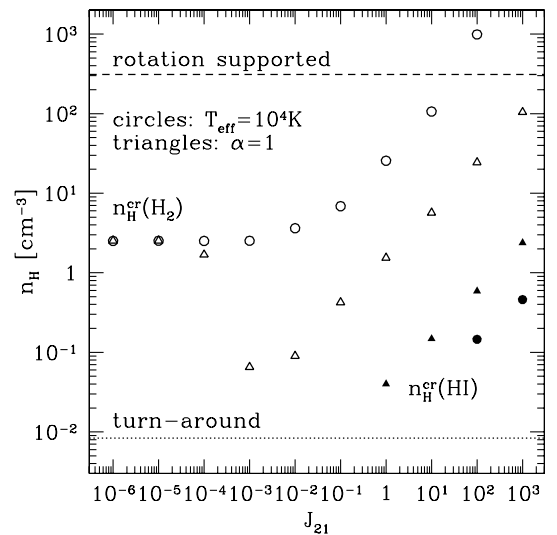


Figure 11. Critical central densities for H_I shielding $n_H^{cr}(HI)$ ($X_{HI} > 0.5$, filled symbols) and H₂ cooling $n_H^{cr}(H_2)$ ($T < 5000$ K, open symbols) versus J_{21} . The spectral shape of the UVB is specified by $\alpha = 1$ (triangles) and $T_{eff} = 10^4$ K (circles). Also plotted for reference are the densities at which the cloud centre turns around (dotted line) and is rotationally supported (dashed line). $V_c = 50$ km s⁻¹ and $z_{c0} = 10$ ($z_c = 3$) are adopted.

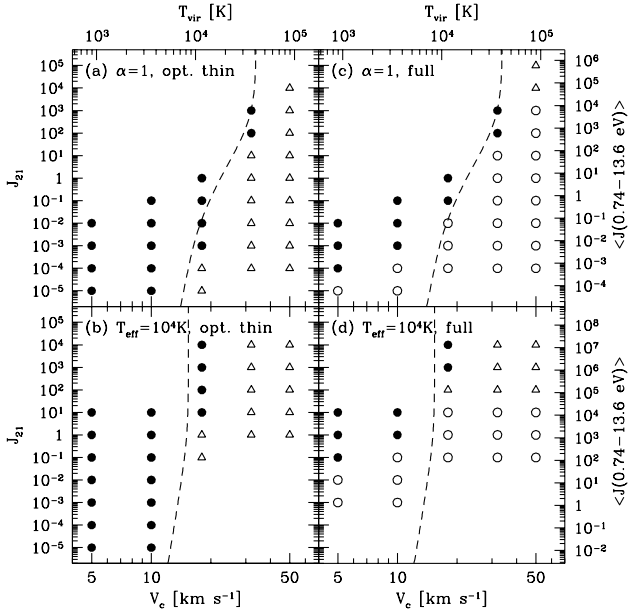


Figure 12. $J_{21} - V_c$ diagram on collapse and cooling of a cloud with $z_{c0} = 10$ ($z_c = 3$). Different panels compare the optically thin (left) and full (right) calculations, and the UV spectrum with $\alpha = 1$ (top) and $T_{\text{eff}} = 10^4$ K (bottom). Symbols indicate whether the cloud centre collapses and the H_2 phase is realized (open circles), collapses but the H_2 phase is not realized (open triangles), or is prohibited to collapse (filled circles). Dashed lines show an analytical estimation for the collapse threshold in the optically thin limit defined in Paper II. The average intensity below the Lyman limit $\langle J(0.74-13.6 \text{ eV}) \rangle$ is displayed on the right vertical axis.

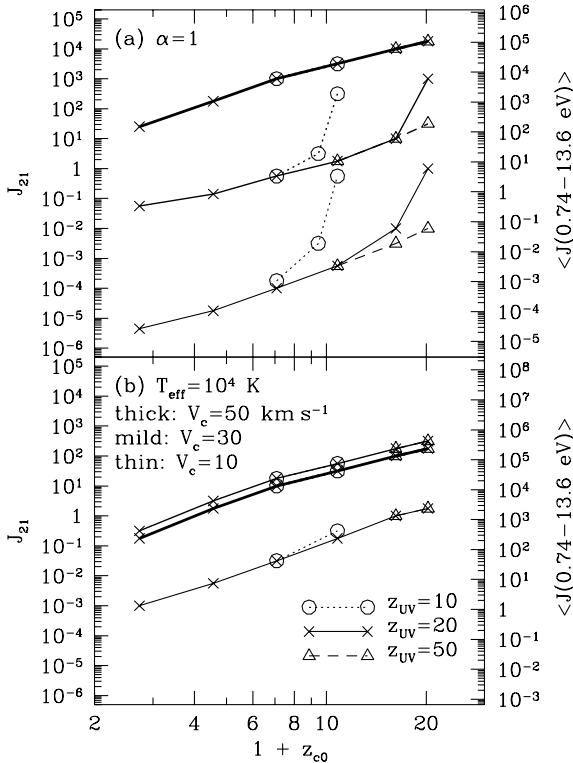


Figure 13. Critical UV intensity above which H_2 cooling is prevented as a function of central collapse redshift z_{c0} : (a) $\alpha = 1$, and (b) $T_{\text{eff}} = 10^4$ K. Circular velocity of a cloud is taken to be $V_c = 50$ (thick lines), 30 (mildly thick lines) and 10 km s^{-1} (thin lines). The onset of the UVB is varied as $z_{\text{UV}} = 10$ (circles, dotted lines), 20 (crosses, solid lines) and 50 (triangles, dashed lines).

contrast, are likely to first undergo sheet-like pancake collapse and evolve in a different manner from the spherical case. They would not end up with the runaway collapse, as the gravity of the sheet is readily overwhelmed by thermal pressure. In fact, Susa & Umemura (2000a,b) argued that the pancakes collapsing in the UVB can bifurcate, depending upon the degree of self-shielding, into observed early- and late-type galaxies. Both their results and ours suggest that the UVB could play an essential role in regulating the star formation history of the Universe.

Recent three-dimensional simulations show that a number of subclumps tend to arise from the fragmentation process in a parent cloud (e.g. Bromm, Coppi & Larson 1999; Abel, Bryan & Norman 2000). The criteria obtained in the current calculations are applicable to each of these locally collapsing subclumps. As a net effect to the parent cloud, the gas clumpiness is likely to enhance self-shielding against the external UVB, because the number of photons necessary to ionize the gas increases roughly by a factor $\langle n_{\text{H}}^2 \rangle / \langle n_{\text{H}} \rangle^2$ (Gnedin & Ostriker 1997; Ciardi et al. 2000b).

Major uncertainties in our predictions are regarding the feedback from the sources formed in an collapsing object. While our simulations can probe directly the cloud evolution until its central collapse, the evolution thereafter will be influenced by several additional processes. For instance, Omukai & Nishi (1999) argued that even a single OB star can photodissociate surrounding hydrogen molecules within a static cloud with $T_{\text{vir}} \lesssim 10^4$ K. On the other hand, Ferrara (1998) pointed out that blow-away processes during supernova explosions can enhance the fraction of hydrogen molecules in surrounding media. Such explosions may also disrupt low-mass objects and induce metal injections into intergalactic space (e.g. Dekel & Silk 1986; Nishi & Susa 1999; Ferrara & Tolstoy 2000). It still remains uncertain to what extent these processes affect successive gas infall and cooling in a dynamically contracting object, the central overdensity of which exceeds $\sim 10^5$. As this issue is beyond the scope of the present paper, we will investigate it separately in our future publications.

5 CONCLUSIONS

We have studied the formation of Population III objects exposed to the external UV radiation. Radiative transfer of photons, H_2 formation and destruction processes and hydrodynamics are incorporated explicitly in our analyses and all shown to play essential roles in the development of Population III objects. Although the UVB does suppress the formation of low-mass objects, the negative feedback turns out to be weaker than previously suggested in the following two respects.

First, the cut-off scale of the collapse drops significantly below $T_{\text{vir}} = 10^4$ K ($V_c = 17 \text{ km s}^{-1}$) at weak UV intensities ($J_{21} \lesssim 10^{-2}$), owing to both self-shielding of the gas and H_2 cooling. Their importance becomes greater at higher redshifts. At stronger intensities, objects as large as $V_c \sim 40 \text{ km s}^{-1}$ can be photoevaporated and prohibited to collapse, in agreement with previous investigations based on the optically thin approximation (e.g. Thoul & Weinberg 1996). High-mass objects well above this scale can collapse almost irrespectively of the UVB by atomic cooling.

Secondly, a spherical cloud that has become Jeans unstable in the UVB tends to undergo runaway collapse and does not settle into hydrostatic equilibrium. As a result, even if the gas is ionized and/or H_2 molecules are destroyed once by radiation at low densities (e.g. Haiman et al. 2000), the radiation is attenuated and H_2 can re-form during the dynamical collapse. The critical

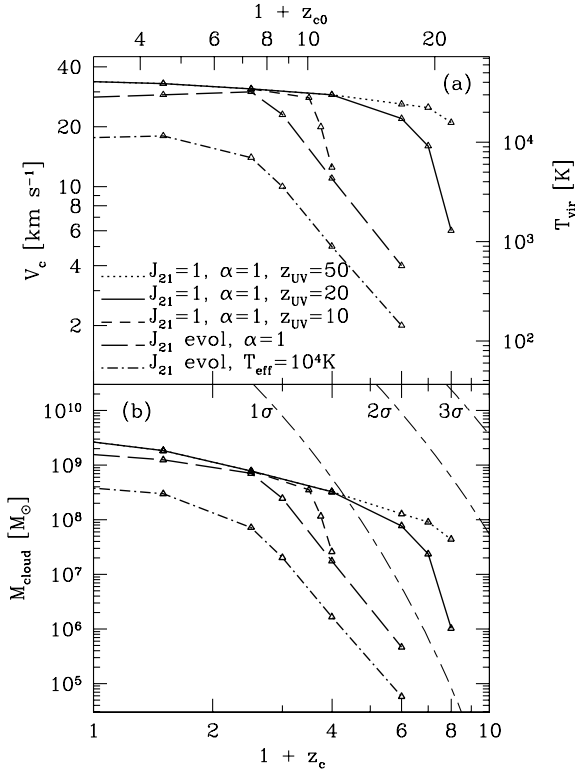


Figure 14. (a) Critical circular velocity, and (b) critical baryon mass, for H_2 cooling as a function of cloud collapse redshift z_c . Lines indicate models on the UVB evolution: (J_{21}, α) = (1, 1) with various onset epochs, $z_{\text{UV}} = 50$ (dotted), 20 (solid) and 10 (short-dashed), and evolving J_{21} (equation 3) with different spectra, $\alpha = 1$ (long-dashed) and $T_{\text{eff}} = 10^4$ K (dot-dashed). Also plotted in panel (b) are the baryon masses and collapse epochs of the 1, 2, 3 σ density perturbations in a Λ CDM model with $(\Omega_0, \lambda_0, h_{100}, \Omega_b, \sigma_8) = (0.3, 0.7, 0.7, 0.05, 1.0)$.

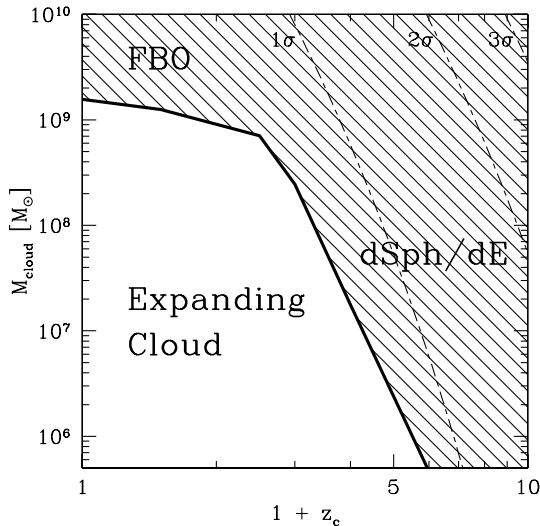


Figure 15. Proposed bifurcation of low-mass objects in the UVB. Objects are classified into expanding clouds, dwarf spheroidal/elliptical (dSph/dE) galaxies, and faint blue objects (FBOs), in terms of their baryonic masses and collapse redshifts. the thick solid line indicates the critical mass for collapse and H_2 cooling in the case of evolving J_{21} (equation 3) with $\alpha = 1$. Also plotted by thin lines are the masses and collapse epochs of the 1, 2, 3 σ perturbations in the Λ CDM model.

densities at which self-shielding and efficient H_2 cooling take place depend sensitively on the spectrum and intensity of the external UVB. For a QSO-like ($\alpha = 1$) spectrum, H_2 formation is even enhanced by a little radiation with $J_{21} \sim 10^{-3}$ – 10^{-2} (Haiman et al. 1996b). For a stellar-like ($T_{\text{eff}} = 10^4$ K) spectrum, H_2 formation is hindered to a greater extent by the photons with energies below 13.6 eV (Haiman et al. 1997). In any case, the collapsing gas is shown to cool efficiently to temperatures well below 10^4 K before it is rotationally supported, as long as the radiation intensity is comparable to or less than $J_{21} \sim 1$ observed at $z \sim 3$. The H_2 fraction in the cooled gas reaches the level $\sim 10^{-3}$, comparable to that achieved commonly in the metal-deficient post-shock layer (Shapiro & Kang 1987; Ferrara 1998; Susa et al. 1998).

Our results imply that star formation can take place in low-mass objects collapsing in the UVB. The threshold baryon mass for the complete suppression of collapse and star formation is $M_{\text{cloud}} \sim 10^9 M_\odot$ at $z_c \lesssim 3$ but drops significantly at higher redshifts. In a conventional Λ CDM universe, it coincides roughly with that of the 1 σ density fluctuations at $z_c \gtrsim 3$. Objects near and above this threshold can thus constitute building blocks of present-day luminous structures, and may also have links to dwarf spheroidal/elliptical galaxies and faint blue objects. These results indicate that the UVB can play a key role in regulating the star formation history of the Universe.

ACKNOWLEDGMENTS

We thank Kuniaki Masai, Taishi Nakamoto and Yukiko Tajiri for discussions, and the referee, Andrea Ferrara, for helpful comments. TK and HS acknowledge support from a Research Fellowships of the Japan Society for the Promotion of Science for Young Scientists and Research Grant of University of Tsukuba Research Project, respectively. This work was partially carried out with facilities at the Center for Computational Physics at University of Tsukuba.

REFERENCES

- Abel T., Haehnelt M. G., 1999, *ApJ*, 520, L13
- Abel T., Norman M. L., Madau P., 1999, *ApJ*, 523, 66
- Abel T., Bryan G. L., Norman M. L., 2000, *ApJ*, 540, 39
- Babul A., Ferguson H. C., 1996, *ApJ*, 458, 100
- Babul A., Rees M. J., 1992, *MNRAS*, 255, 346
- Bajtlik S., Duncan R. C., Ostriker J. P., 1988, *ApJ*, 327, 570
- Barkana R., Loeb A., 1999, 523, 54
- Barns J., Efstathiou G., 1987, *ApJ*, 319, 575
- Bechtold J., 1994, *ApJS*, 91, 1
- Bertschinger E., 1985, *ApJS*, 58, 39
- Bond J. R., Szalay A. S., Silk J., 1988, *ApJ*, 324, 627
- Bowers R. L., Wilson J. R., 1991, *Numerical Modelling in Applied Physics and Astrophysics*. Jones & Bartlett, Boston
- Bromm V., Coppi P. A., Larson R. B., 1999, *ApJ*, 527, L5
- Chiba M., Nath B. B., 1994, *ApJ*, 436, 618
- Ciardi B., Ferrara A., Abel T., 2000a, *ApJ*, 533, 594
- Ciardi B., Ferrara A., Governato F., Jenkins A., 2000b, *MNRAS*, 314, 611
- Ciardi B., Ferrara A., Marri S., Raimondo G., 2001, *MNRAS*, 324, 381
- Cooke A. J., Espey B., Carswell R. F., 1997, *MNRAS*, 284, 552
- Corbelli E., Galli D., Palla F., 1997, *ApJ*, 487, L53
- Couchman H. M. P., 1985, *MNRAS*, 214, 137
- Cowie L. L., Lilly S. J., Gardner J. P., McLean I. S., 1988, *ApJ*, 332, L2
- Dekel A., Silk J., 1986, *ApJ*, 303, 39
- Draine B. T., Bertoldi F., 1996, *ApJ*, 468, 269
- Efstathiou G., 1992, *MNRAS*, 256, 43
- Efstathiou G., Jones B. J. T., 1979, *MNRAS*, 186, 133

- Ellis R., 1997, *ARA&A*, 35, 389
- Ferrara A., 1998, *ApJ*, 499, L17
- Ferrara A., Tolstoy E., 2000, *MNRAS*, 313, 291
- Fukugita M., Kawasaki M., 1994, *MNRAS*, 269, 563
- Galli D., Palla F., 1998, *A&A*, 335, 403
- Giallongo E., Cristiani S., D'Odorico S., Fontana A., Savaglio S., 1996, *ApJ*, 466, 46
- Gnedin N. Y., 2000a, *ApJ*, 535, L75
- Gnedin N. Y., 2000b, *ApJ*, 535, 530
- Gnedin N. Y., Ostriker J. P., 1997, *ApJ*, 486, 581
- Gunn J. E., Peterson B. A., 1965, *ApJ*, 142, 1633
- Haiman Z., Thoul A. A., Loeb A., 1996a, *ApJ*, 464, 523
- Haiman Z., Rees M. J., Loeb A., 1996b, *ApJ*, 467, 522
- Haiman Z., Rees M. J., Loeb A., 1997, *ApJ*, 476, 458
- Haiman Z., Abel T., Rees M. J., 2000, *ApJ*, 534, 11
- Hirasawa T., 1969, *Prog. Theor. Phys.*, 42, 523
- Ikeuchi S., 1986, *Ap&SS*, 118, 509
- Kang H., Shapiro P., 1992, *ApJ*, 386, 432
- Kepner J., Babul A., Spergel N., 1997, *ApJ*, 487, 61
- Kitayama T., Ikeuchi S., 2000, *ApJ*, 529, 615, (Paper I)
- Kitayama T., Suto Y., 1996, *ApJ*, 469, 480
- Kitayama T., Tajiri Y., Umemura M., Susa H., Ikeuchi S., 2000, *MNRAS*, 315, L1, (Paper II)
- Lee J. C., Salzer J. J., Law D. A., Rosenberg J. L., 2000, *ApJ*, 536, 606
- Machacek M. E., Bryan G. L., Abel T., 2001, *ApJ*, 548, 509
- Mateo M., 1998, *ARA&A*, 36, 435
- Matsuda T., Sato H., Takeda H., 1969, *Prog. Theor. Phys.*, 42, 219
- Miralda-Escudé J., Ostriker J. P., 1990, *ApJ*, 350, 1
- Murakami I., Ikeuchi S., 1993, *ApJ*, 409, 42
- Nakamoto T., Umemura M., Susa H., 2001, *MNRAS*, 321, 593
- Nishi R., Susa H., 1999, *ApJ*, 523, L103
- Omukai K., Nishi R., 1999, *ApJ*, 518, 64
- Osterbrock D. E., 1989, *Astrophysics of Gaseous Nebulae and Active Galactic Nuclei*. University Science Books, Mill Valley
- Pascarelle S. M., Windhorst S. P., Keel W. C., Odewahn S. C., 1996, *Nat*, 383, 45
- Peebles P. J. E., 1980, *The Large-Scale Structure of the Universe*. Princeton Univ. Press, Princeton
- Peebles P. J. E., Dicke R. H., 1968, *ApJ*, 154, 891
- Razoumov A. O., Scott D., 1999, *MNRAS*, 309, 287
- Rees M. J., 1986, *MNRAS*, 218, 25, p
- Sasaki S., Takahara F., 1994, *Prog. Theor. Phys.*, 91, 699
- Schmalzing J., Sommer-Larsen J., Götz M., 2000, *ApJ*, submitted (astro-ph/0010063)
- Shapiro P. R., Kang H., 1987, *ApJ*, 318, 32
- Stancil P. C., 1994, *ApJ*, 430, 360
- Stecher T. P., Williams D. A., 1967, *ApJ*, 149, L29
- Susa H., Kitayama T., 2000, *MNRAS*, 317, 175
- Susa H., Umemura M., 2000a, *ApJ*, 537, 578
- Susa H., Umemura M., 2000b, *MNRAS*, 316, L17
- Susa H., Uehara H., Nishi R., Yamada M., 1998, *Prog. Theor. Phys.*, 100, 63
- Tajiri Y., Umemura M., 1998, *ApJ*, 502, 59
- Tajiri Y., Umemura M., 2001, *MNRAS*, submitted
- Tegmark M., Silk J., Rees M. J., Blanchard A., Abel T., Palla F., 1997, *ApJ*, 474, 1
- Thoul A. A., Weinberg D. H., 1995, *ApJ*, 442, 480
- Thoul A. A., Weinberg D. H., 1996, *ApJ*, 465, 608
- Thuan T. X., Martin G. E., 1981, *ApJ*, 247, 823
- Tscharnutter W. M., Winkler K.-H., 1979, *Comp. Phys. Commun.*, 18, 171
- Tyson J. A., 1988, *AJ*, 96, 1
- Umemura M., Ikeuchi S., 1984, *Prog. Theor. Phys.*, 72, 47
- Umemura M., Nakamoto T., Susa H., 2000, in Sato K., Kawasaki M. eds, *The Birth and Evolution of the Universe*. Universal Academy Press, Tokyo, p. 297
- Wang L., Caldwell R. R., Ostriker J. P., Steinhardt P. J., 2000, *ApJ*, 530, 17
- Warren M. S., Quinn P. J., Salmon J. K., Zurek W. H., 1992, *ApJ*, 399, 405
- Zhang Y., Anninos P., Norman M. L., 1995, *ApJ*, 453, L57

This paper has been typeset from a \LaTeX file prepared by the author.